



Innovative Approach to Evaluate the Mechanical Performance of Ti–6Al–4V Lattice Structures Produced by Electron Beam Melting Process

Giuseppe Del Guercio¹ · Manuela Galati^{1,3} · Abdollah Saboori^{2,3} 

Received: 2 March 2020 / Accepted: 23 April 2020 / Published online: 25 May 2020
© The Korean Institute of Metals and Materials 2020

Abstract

Additive manufacturing processes allow producing complex geometries which include structures with enhanced mechanical performance and biomimetic properties. Among these structures, the interests on the use of lattice are increasing for both medical and mechanical applications. The mechanical behaviour of the structure is closely correlated to its shape and dimension. However, up to now, far too little attention has been paid to this aspect. Hence, this work aims to explore the effect of geometry, dimension and relative density of the cell structure on the compressive strength of specimens with lattice structures. For this purpose, various Lattice structures are designed with different geometries and dimensions. This approach leads to having structures with different relativity densities. Replicas of the designed structure are produced using Ti–6Al–4V powder processed by electron beam melting process. The samples are tested under compression. A new approach to calculate the absorbed energy up to failure by the lattice structure is presented. The results show a close relationship between the mechanical performance of the structure and the investigated parameters. In contrast with the current literature, the presented experimental data and a collection of the literature data highlight that the lattice structures with similar relative density do not exhibit the same Young's modulus values.

Keywords Electron beam melting · Lattice · Ti–6Al–4V · Mechanical performance · Absorbed energy

1 Introduction

Additive manufacturing (AM) is defined as “a process of joining materials to obtain components from 3D model data using a layer upon layer approach” [1–3]. This approach allows the production of free design constraints parts, enabling the construction of both integrated parts, lightweight and topologically optimized structures [4, 5]. Especially for metal components, AM has become primarily applied in

various industries [6, 7]. In general AM processes can be classified in two main groups; powder bed fusion (PBF) and Directed Energy Deposition (DED) [8]. Among the metal AM techniques, a great interest has been developed around the electron beam melting (EBM) process, which is already used for mass production in the aerospace and medical applications [9]. For aerospace, the main drivers are the possibility to work with materials for which other manufacturing techniques suffer from several limitations [10]. For the medical sector, implants can be tailored to allow better biocompatibility and improve the interaction with prior tissues [11]. Ti–6Al–4V alloy is the material which is significantly processed via EBM technology, mainly owing to the possibility to overcome the limitations of the traditional manufacturing technologies [12]. This interest is primarily due to the necessity to erase high-density inclusions (HDI) and low-density inclusions (LDI), to avoid the surface oxidation, especially at high temperatures, and to guarantee the composition homogeneity [13]. Thanks to the vacuum environment and the preheating phase that precedes the melting phase [12], the temperature inside the chamber reaches the high

✉ Abdollah Saboori
abdollah.saboori@polito.it

¹ Department of Management and Production Engineering (DIGEP), Politecnico Di Torino, Corso Duca degli Abruzzi 24, 10129 Turin, Italy

² Department of Applied Science and Technology (DISAT), Politecnico Di Torino, Corso Duca degli Abruzzi 24, 10129 Turin, Italy

³ Integrated Additive Manufacturing Center (IAM) @ Polito, Politecnico Di Torino, Corso Duca degli Abruzzi 24, 10129 Turin, Italy

temperatures. For instance, this temperature for Ti–6Al–4V alloy is around 650–700 °C [14, 15]. This feature ensures small thermal shrinkages and a certain strength of the powder bed prior to the melting phase because it reaches a high grade of consistency [16]. For this reason, the EBM process requires a small number of supports and the construction of micro-architected materials, such as the lattice structures, is easier. Micro-architected materials which are also known as cellular materials have been largely studied due to their possibility to achieve a unique combination of being light structure and having high mechanical properties with respect to their corresponding bulk materials [17, 18]. More specifically, lattice structures made of Ti–6Al–4V alloy which have been produced by the EBM process exhibit interesting properties such as high specific strength [19], oxidation resistance [19, 20] and biocompatibility with the human tissues [11, 20, 21]. Lattice structures, which are also called cellular, reticulated or truss, are defined as structures that can be produced via the repetition of a unit cell throughout a space [17]. Ashby identified three main factors that influence the properties of cellular solids: (1) the material of which is made, (2) the cell topology and shape, and (3) the relative density [22]. In fact, the material affects the mechanical, thermal and electrical properties of the cellular solid. Instead, the cell topology and the shape distinguish a bending dominated structures from a strength dominated one [23]. The relative density is calculated by the ratio between the density of the cellular material (ρ^*) and the density of the bulk one (ρ_s) [24]. As a matter of fact, the topology of the cell and its relative density strongly affect the cooling rate of the material during its solidification and also the load distribution during the working conditions. A high cooling rate leads to the formation of a microstructure that, in contrast with the bulk material [14, 19, 25–32], consists of α' -martensite. So far, several works have been focused on the evaluation of the performance of the lattice structure. For instance, Murr et al. [19] and Cheng et al. [32] evaluated the compressive Young's modulus of lattice structures at different relative densities using the resonant frequency method and the damping analysis. Van Grunsven et al. [33] studied a diamond unit cell with graded relative density. The total compressive stiffness of the graded structures has been found to be influenced by the compressive stiffness of each layer of the lattice. Jamshidinia et al. [34] evaluated the application of three different unit cells (cross, honeycomb and octahedral) with two similar cell sizes. Indeed, those findings have been used to calibrate a numerical model which simulated a dental implant. Xiao et al. [35] studied the compressive behaviour of open-cell rhombic dodecahedron structures with two different ratios between the length of the strut and its diameter. As observed by Ashby and

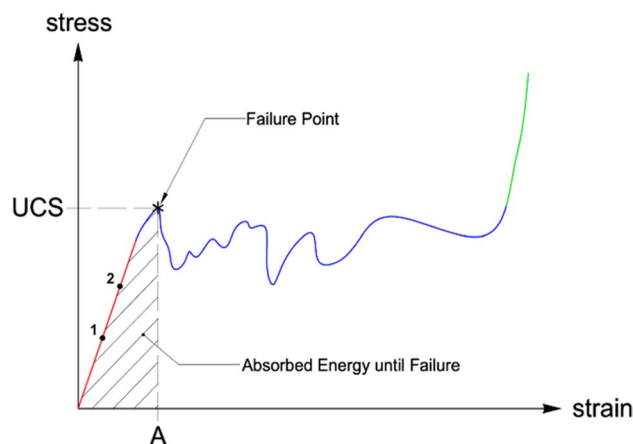


Fig. 1 A typical compressive behaviour of a generic lattice structure. (Color figure online)

Gibson [24], all studies showed that lattice structures under compressive load at room temperature exhibit a compressive behaviour characterised by three main stages (Fig. 1): (1) elastic behaviour of the lattice structure (red line), (2) progressive collapse of the layers (blue line) up to the structure has (3) the same behaviour of the bulk material (green line). As can be seen, in the beginning, the lattice structure has an elastic behaviour. Thereafter, progressive collapse of the layers can be observed up to a deformed structure as same as the behaviour of the bulk material. Typically, the failure mode in these sort of components is a brittle fracture at 45° [31, 32, 36–39]. The first maximum of the compressive curve identifies the failure point of the structure (Star in Fig. 1). The failure point corresponds to the ultimate compressive strength (UCS^*) and the elongation at failure (A^*).

Lattice structure with larger cell size showed worse compressive performances in comparison with those manufactured with smaller cell size [34, 38, 40] in terms of Young's modulus and UCS. Ashby and Gibson [24], to describe the mechanical properties of such structures, proposed a model in which a generic relative property (defined as the ratio between the lattice properties and the corresponding bulk one) can be expressed as a linear relationship of the lattice relative density in a bi-logarithmic diagram. That model has been used in several studies [19, 27, 31, 32, 36, 37, 40–43] to fit the experimental mechanical properties of the investigated structure. All studies have found a constant deviation between the experimental results and the Ashby and Gibson model. This deviation has been usually attributed to the differences between the investigated structure. However, most of the studies have been investigated the relationship between a single cell topology and a unique cell size. Nonetheless, in these investigations, the role of the geometry of

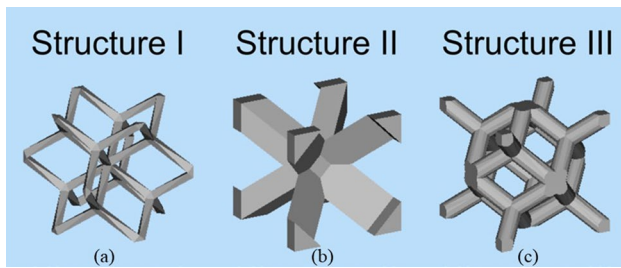


Fig. 2 Three different unit cells used in the present study; **a** structure I: Dode Thin, **b** structure II: G-Structure 3, **c** structure III: Rombi Dodecahedron

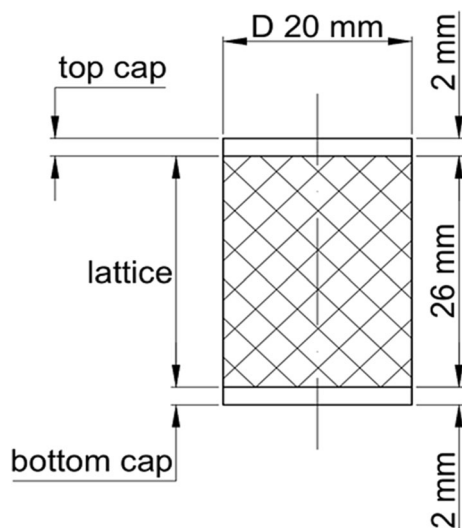
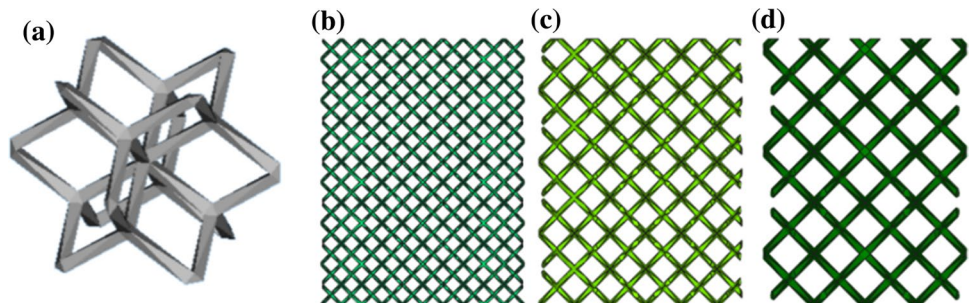


Fig. 3 The general design of each specimen for the compression test

the cell on the mechanical properties of the cellular structure is rarely considered. Hence, the aim of this work is to fill this gap and study the correlation between the cell geometry and mechanical characteristic of cellular structures made of Ti–6Al–4V alloy. For this reason, three different cell topologies with three different sizes are considered, designed and produced via the EBM process. In fact, in this sort of design of experiments, it is possible to design the structures with different relative porosities and then study its relationship with the mechanical performance of the cellular structure.

Fig. 4 An example of the designed sample for the structure I: **a** elementary structure and topography of the lattice with size, **b** 4 mm, **c** 7 mm and **d** 10 mm



2 Design of Experiments

2.1 Lattice Design

In this study, the behaviour of three different unit cell topologies have been analysed: (I) Dode Thin, (II) G-Structure 3, (III) Rombi Dodecahedron. Figure 2 depicts the topology of the aforementioned unit cells.

All the structures have been selected among the standard lattice cells presented in the database of the Materialise Magics 21.11. The chosen primary cell allows analysing different relative densities and struts sizes. The compressive samples (Fig. 3) had a cylindrical shape with a diameter and a height equal to 20 and 30 mm, respectively. In order to provide a uniform distribution of the load during the compression test, the lattice structures were designed between two bulk disks with a thickness of 2 mm. Thus, the total height of the lattice structure, without the consideration of two thin disks, was 26 mm. Each unit cell has been designed with three different sizes: 4, 7 and 10 mm. Figure 4 shows an example of Structure I.

Table 1 lists the geometrical characteristics of each structure.

2.2 Production

In order to guarantee a robust experimental analysis, for each cell typology and size, three replicas have been produced. Besides, some bulk specimens have also been designed to evaluate the actual density of the Ti–6Al–4V made by the EBM process. The replicas were orientated so that the larger surface of the resulted cups were placed parallel to the start plate. All replicas have been produced unattached to the start plate and supported by proper structure to avoid microstructure modifications.

Additionally, they have been conveniently spaced along the building axis to have a uniform temperature distribution during the building phase. The build job was prepared using Magics 21.1. The build job has been processed by the EBM build processor 5.0 with Ti–6Al–4V standard theme for the Arcam A2X system and layer thickness of

Table 1 Geometrical features of each structure; all the values have been extracted from the magics file

Structure	Cell size (mm)	Strut size (mm)	Strut length (mm)
I	4	0.297	1.732
	7	0.519	2.601
	10	0.734	3.755
II	4	0.809	1.091
	7	1.432	1.884
	10	2.000	2.736
III	4	0.704	1.410
	7	1.382	2.467
	10	1.442	3.418

Table 2 The process parameters used in this work to produce the lattice structures

	Scan speed (mm/s)	Focus offset (mA)	Max Beam current (mA)	Number of contours	Hatch contours (mm)
Outer contour	450	0	3	1	0.13
Inner contour	470	0	3	1	0.13

50 μm . The samples were produced using an Arcam A2X system with standard Arcam Ti–6Al–4V powder with an average size of 75 μm . The process parameters used in this study are listed in Table 2.

After the production, the entire build has been cooled down inside the EBM chamber up to the room temperature. Thereafter, all specimens have been cleaned from the residual powders by a blasting process with compressed air at 4 bar and the Ti–6Al–4V powders. To verify the blasting process, after a careful powder removal, all the samples have been analysed by a Stereomicroscope. Figure 5 depicts representative images for each sample after the blasting process.

2.3 Compression Test

To evaluate the effect of cell type and cell size on the mechanical performance of Ti–6Al–4V lattice specimens the uniaxial compression test using a strain velocity of 2 mm/min up to the full collapse of the structure has been selected. For specimens of the same unit cell type and unit cell size, similar loads/displacements trends have been observed. To calculate the stress/strain curves according to the load/displacement curves, Eqs. 1 and 2 have been used:

$$\sigma = \frac{P}{A_0} \quad (1)$$

$$\varepsilon = \frac{\delta}{l_0} \quad (2)$$

where P is the load and δ is the displacement during the compression test; A_0 is the area of the whole structure considered as the area of a circle of 20 mm diameter, while l_0 is the height of the lattice part of each sample which is 26 mm.

The area under the curve and delimited by the failure point is the absorbed energy up to failure per volume unit. W^* represents the absorbed energy up to failure by the lattice structure and can be calculated as follows:

$$W^* = \int_0^{A^*} \sigma d\varepsilon \cdot V^* \quad (3)$$

In Eq. 3, V^* is the ratio between the mass of the structure and the nominal density of the material.

The compressive Young's modulus E^* can be evaluated calculating the slope of a straight line between two points (e.g. 1 and 2 in Fig. 1) on the linear part of the curve:

$$E^* = \frac{\sigma_2 - \sigma_1}{\varepsilon_2 - \varepsilon_1} \quad (4)$$

2.4 Characterization

By subtracting the mass of the upper and bottom cup from the total weight of the sample, the relative density of each structure, ρ^*/ρ_s , is evaluated by the ratio between the density of the lattice structure (ρ^*) and the nominal density of the material (ρ_s). Table 3 resumes the measured and calculated data for each cell topology and cell size.

For microstructure observation, the samples were firstly cut, then mount, ground and finally polished according to the standard procedure for the metallography of Ti alloys. Thereafter, the as-polished samples were etched using Kroll's reagent (2% HF, 4% HNO₃ in distilled water). A Leica Stereomicroscope was used to evaluate the morphology of the lattice structures from the macroscopic point of view. A Phenom table-top Scanning Electron Microscope (SEM) equipped with an EDS detector was employed to evaluate the microstructure of as-built samples.

3 Results and Discussion

Figure 6 shows the deformation mechanism of the lattice structure. As expected, the stress progressively raises as the strain increases. When the structure reaches the failure point, the stress drops down because of the effect of the

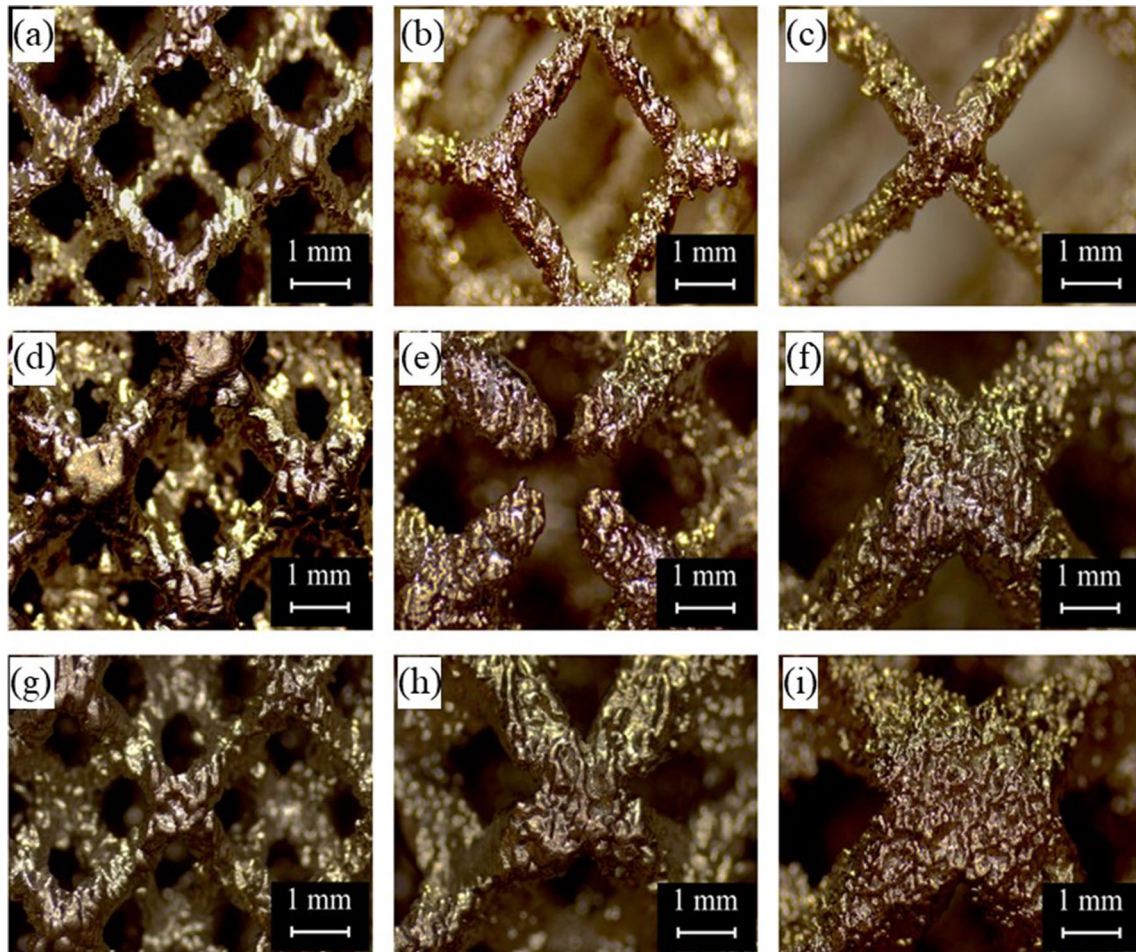


Fig. 5 Representative stereomicroscope images of each specimen; **a–c** structure I with the unite cell of 4, 7 and 10 mm, **d–f** structure II with the unite cell of 4, 7 and 10 mm and **g–i** structure I with the unite cell of 4, 7 and 10 mm

Table 3 Average values of the weight of the lattice and relative densities

Structure	I			II			III		
Cell size (mm)	4	7	10	4	7	10	4	7	10
m_{latt} (g)	5.832	3.139	2.018	12.016	7.512	6.806	10.298	9.697	8.887
ρ^*/ρ_s (%)	16.155	8.695	5.591	33.283	20.808	18.852	28.523	26.859	24.615
V^* (mm ³)	1319.532	710.180	456.661	2718.602	1699.622	1539.869	2329.839	2193.841	2010.583

failure mechanism of the structure. The failure mode consists of a brittle fracture which occurred at 45° with respect to the horizontal plane for the samples with the incomplete cells. The subsequent strain increase leads to stress increase up to the point where all the elementary cells of the structure are completely collapsed, and after that, the sample behaves like a bulk material. In general, the curve is characterised by recurring twitches. This can be explained considering that the lattice in the as-built condition can be compared to a brittle foam. In fact, when a single strut

of the whole structure is collapsed, the load would drop suddenly [24]. As shown in Fig. 5, due to maintaining the same geometry for all the samples by varying the cell type and cell size there is some incomplete cells in the sample produced using structure II and unit cell size of 7 mm. As can be seen in Fig. 6, this incomplete cells can results in the failure of samples at 45° with a marked drop in the stress after the UCS. Whereas, in other samples without incomplete cells, the failure at 45° followed by a significant stress drop after UCS was negligible.

Fig. 6 The compressive trend for structure II with a unit cell size of 7 mm

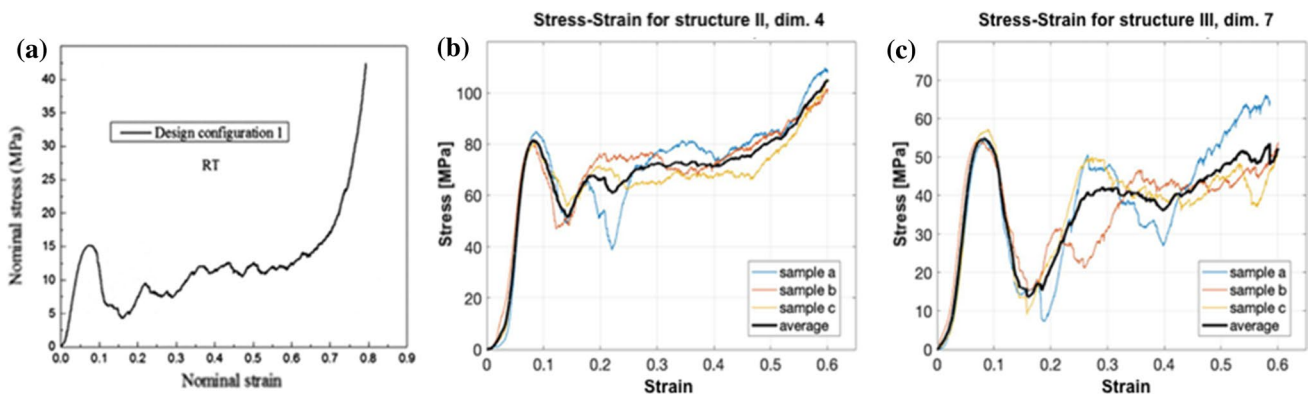
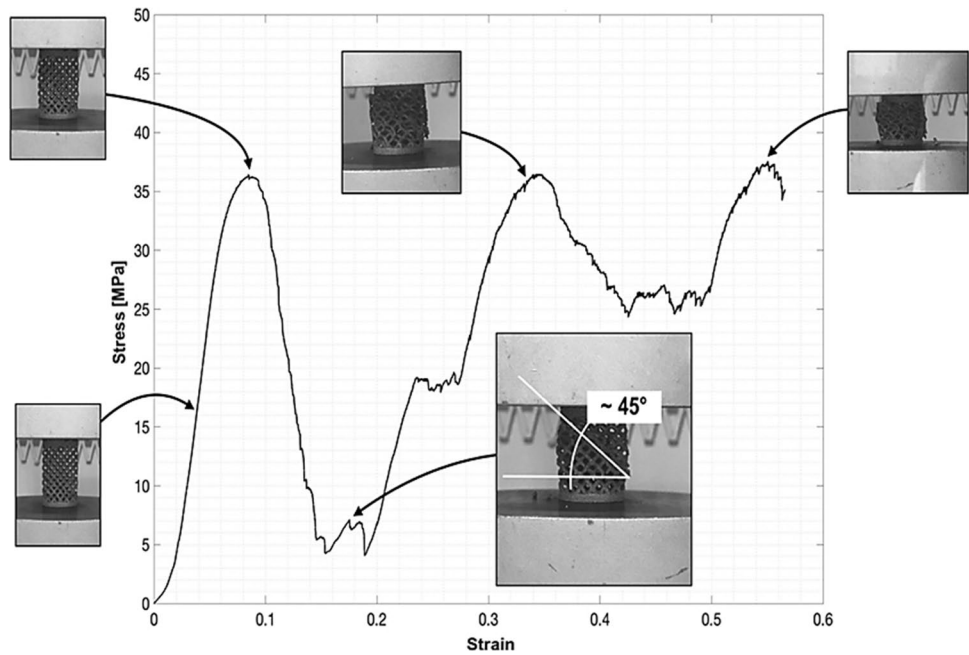


Fig. 7 Trends observed in the literature by Xiao et al. [35] a, for structure II-4 b and for structure III-7 c

Table 4 The average characteristics of the different unit cell types and sizes

Structure	Cell size (mm)	E* (GPa)	UCS* (MPa)	A* (%)	W* (kJ)
I	4	0.339 ± 0.030	19.145 ± 0.546	10.947 ± 0.171	1.532 ± 0.051
	7	0.074 ± 0.004	4.742 ± 0.122	10.644 ± 0.820	0.201 ± 0.028
	10	0.036 ± 0.003	2.262 ± 0.090	11.951 ± 0.598	0.081 ± 0.006
II	4	2.264 ± 0.331	81.882 ± 2.349	8.231 ± 0.393	7.321 ± 0.404
	7	0.717 ± 0.114	32.435 ± 2.395	7.392 ± 1.225	2.248 ± 0.357
	10	0.659 ± 0.084	28.665 ± 1.493	7.973 ± 0.420	1.804 ± 0.256
III	4	1.560 ± 0.045	60.034 ± 1.025	8.077 ± 0.884	4.837 ± 0.357
	7	1.285 ± 0.116	54.877 ± 1.579	8.331 ± 0.777	4.964 ± 0.484
	10	0.967 ± 0.190	39.691 ± 1.283	7.186 ± 1.247	2.836 ± 0.280

Figure 7 shows the comparison between a typical compression curve for a lattice structure (Fig. 7a) [35] and all experimental curves for the structure II with a unit cell size of 4 mm (Fig. 7b) and for structure III with a unit cell size of 7 mm (Fig. 7c). The black line represents the mean trend of the three replicas. As can be seen, the obtained curves in this work are in good agreement with the findings in the literature. Additionally, for each cell size, all three compressive curves are similar, especially in the first segment, before the first drop in load.

Owing to the high repeatability, the average values have been considered for the analysis and Table 4 resumes the average of the abovementioned mechanical properties for each structure. For the sake of clarity in the subsequent discussion, the deviation from the average values is also reported.

3.1 Effects of Cell Type and Size

Figure 8 shows the effect of the cell size on the values of E^* , UCS^* and W^* with the relative deviation from the average value for the structure I. As can be seen, an increment in the unit cell size leads to a reduction of the mechanical properties. Nonetheless, Table 4 shows that A^* did not change markedly with increasing the strut size for all the lattice structure. It is interesting to notice that these trends in the mechanical strength and elongation at failure of lattice samples with the structure I, are also consistent for both structures II and III.

Figure 9 depicts the effects of the unit cell type on the samples designed with a 4 mm unit cell size. The structure I showed the worst mechanical performance, while structure II was the best one. On the other hand, the structure I showed

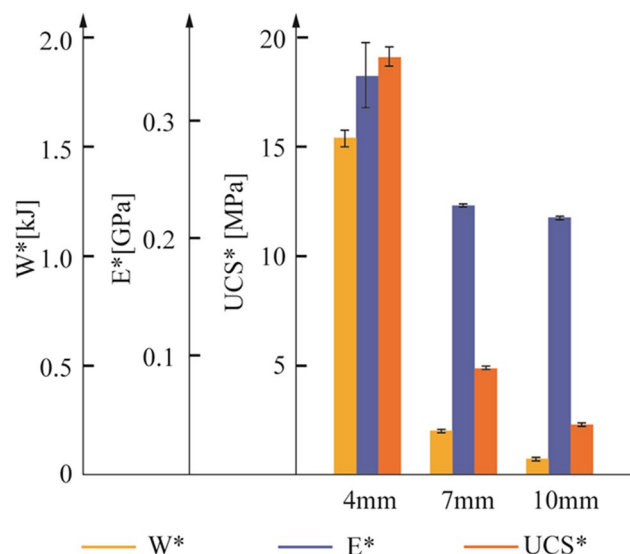


Fig. 8 The main mechanical properties for the specimens designed with the structure I in all the three-unit cell sizes

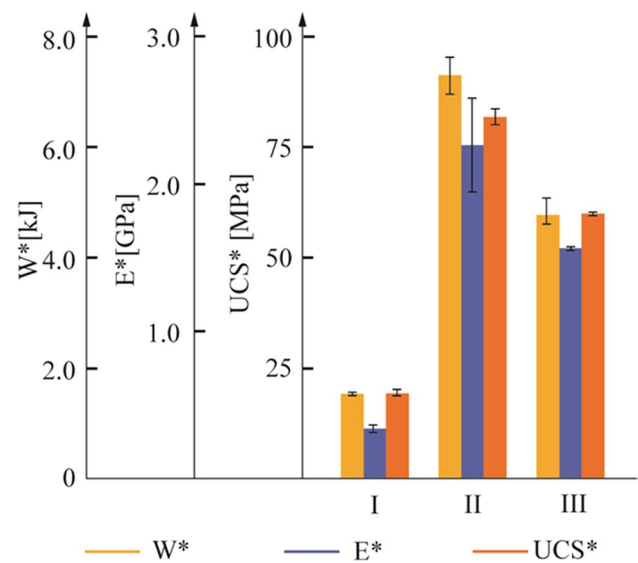


Fig. 9 The main mechanical properties for the specimens designed with the 4 mm unit cell size in all the three structure types

the greatest A^* value. These kinds of trends have not been observed analysing the samples designed with the 7 mm and 10 mm unit cell sizes. This suggests that between the two analysed design features, the unit cell size plays a much more significant role in the mechanical strength of the lattice structures. Moreover, the variations of A^* with the cell type and cell size that have been shown in Table 4, shows no clear dependence with the cell size. However, it is found that A^* decreased slightly for the structure II and III that has a more relative density with respect to the structure I. This discrepancy in the A^* can be related to several factors such as the relative density, microstructure, residual internal and surface defects and surface roughness of the lattice structures.

However, according to the Ashby and Gibson theory, an obvious trend in the mechanical properties should be observed if the relative density is considered as the main factor. Figure 10 shows the mechanical properties and their deviation for each structure ordered according to its relative density (Table 3).

As far as Young's modulus is concerned, the structure I-10 has the lowest relative density and shows the minimum of Young's modulus values (0.036 GPa). On the other hand, the structure II-4 has the highest relative density and shows the highest Young's modulus (2.264 GPa) as well as the highest deviation. In fact, in this case, the effect of open cells is significant for the mechanical response of the structure. The same result has been found valid for the UCS^* and W^* . In general, it is found that the mechanical strength of the lattice structures is increased by increasing their relative density. According to the Ashby and Gibson model [24], the relationship between Young's modulus and the relative density is expressed by the following equation:

Fig. 10 Variation of the mechanical properties according to the relative density of the structure

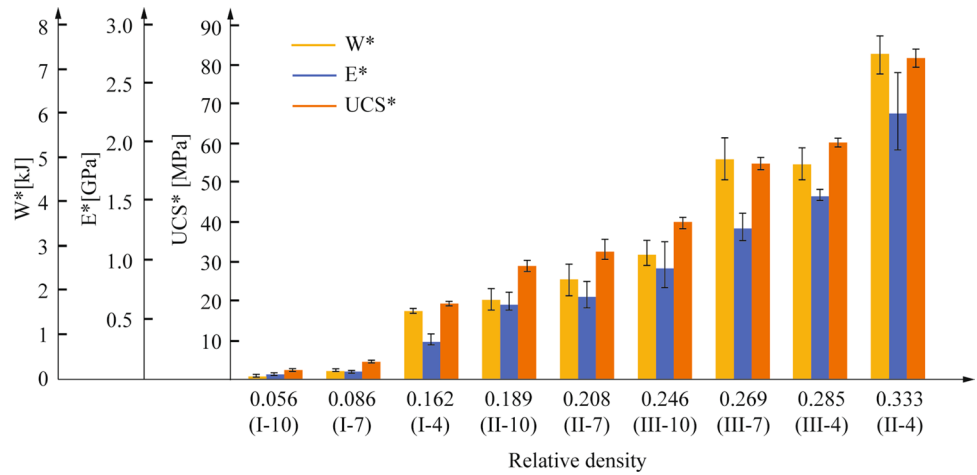
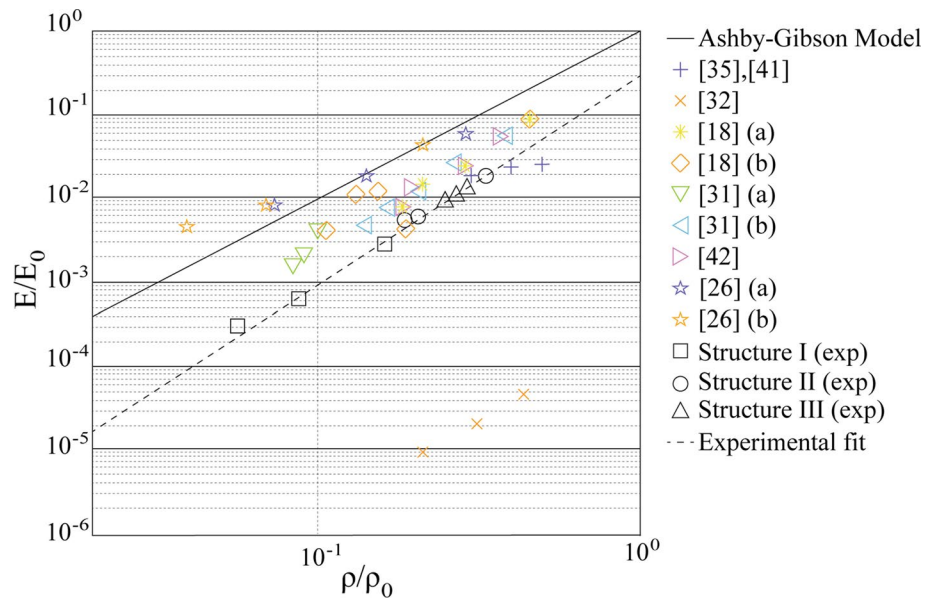


Fig. 11 Bi-logarithmic diagram of the relative Young’s modulus as a function of the relative density



$$\frac{E^*}{E_s} = C_1 \left(\frac{\rho^*}{\rho_s} \right)^n \tag{5}$$

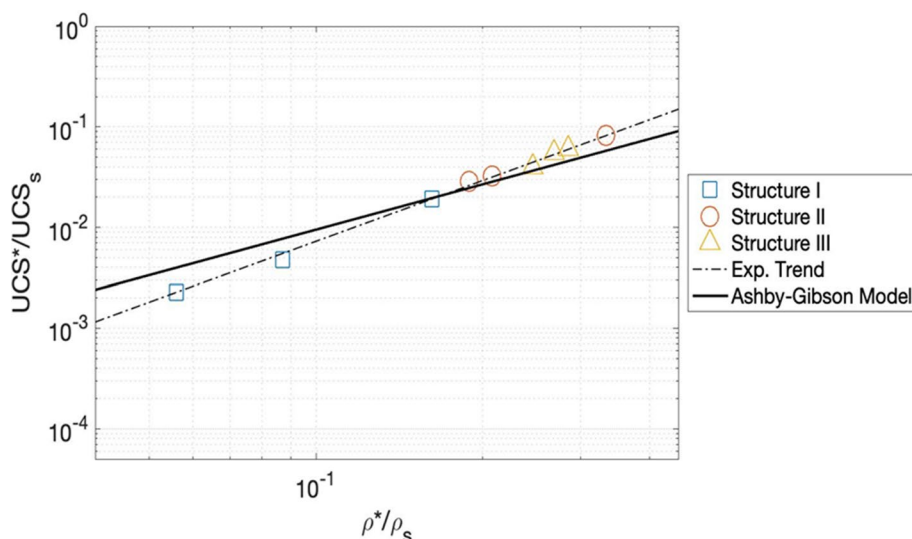
where E^* is the stiffness of the cellular material, E_s is the stiffness of the bulk material, that for the bulk Ti–6Al–4V alloy was chosen equal to 120 GPa [44], and C_1 and n are constant equal to 1 and 2, respectively. Equation 5 can be represented in a bi-logarithmic diagram as a straight line (black line in Fig. 11). The experimental results are also depicted in Fig. 11. In fact, they indicated a constant deviation from the theoretical values, which are always higher. An interpolation (dotted line in Fig. 11) of the experimental data showed that the data are still following a like Ashby and Gibson model in which the constant of the experimental law and the exponent of the relative density are equal to 0.301 and 2.493, respectively. This could be explained with the

fact that structures made by repetitive pattern or cells (lattice structure). As a matter of fact, these cells are characterised by sharp edges and consequently work as stress concentration points that results in the lowering of the lattice stiffness with respect to the stochastic structures (foams) which have been investigated by Ashby and Gibson [24]. Similarly, Eq. 6 defined the relationship between the UCS^* and the relative density:

$$\frac{UCS^*}{UCS_s} = C_5 \left(\frac{\rho^*}{\rho_s} \right)^m \tag{6}$$

where UCS^* is the Ultimate Compressive Strength of the cellular material, UCS_s is the Ultimate Compressive Strength of the bulk material (assumed equal to 1000 MPa for Ti–6Al–4V alloy); lastly, C_5 and n are constant equal

Fig. 12 Bi-logarithmic diagram showing the relationship between the relative UCS and the relative density



to 0.3 and 2, respectively [24]. Differently from Young’s modulus, the collected experimental data are closer to the Ashby-Gibson law (Fig. 12). Regarding the experimental trend, the value of the C_5 and m are equal to 0.744 and 2.012, respectively, which are in line with previous works [36, 42].

Regarding the absorbed energy, this property has been evaluated, as mentioned before, up to the cited failure point. In addition, it is found that the variation of the absorbed energy by changing the density is also followed the trend that has been proposed Ashby and Gibson model for the mechanical properties of the lattice structures. As previously shown, the relative absorbed energy can be considered as the ratio between the energy absorbed by the lattice structure (W^*) and the energy absorbed by the bulk material (W_s) which can be evaluated as follows:

$$W_s = \frac{1}{2} \cdot \frac{UCS_s^2}{E_s} \cdot V_s \tag{7}$$

An empirical law that fits the experimental can be obtained and is expressed by the following equation:

$$\frac{W^*}{W_s} = 3.153 \left(\frac{\rho^*}{\rho_s} \right)^{2.472} \tag{8}$$

As expected, the variation in the relative absorbed energy seems to be in a good agreement with the relative density (Fig. 13).

In Fig. 11, in addition to the discussed experimental results of this study, the results of previous investigations are included. The comparison between the outcomes of this study and the literature data indicated that the structures with the same relative density exhibit different values of the

Fig. 13 Bi-logarithmic diagram showing the relationship between the relative absorbed energy and the relative density

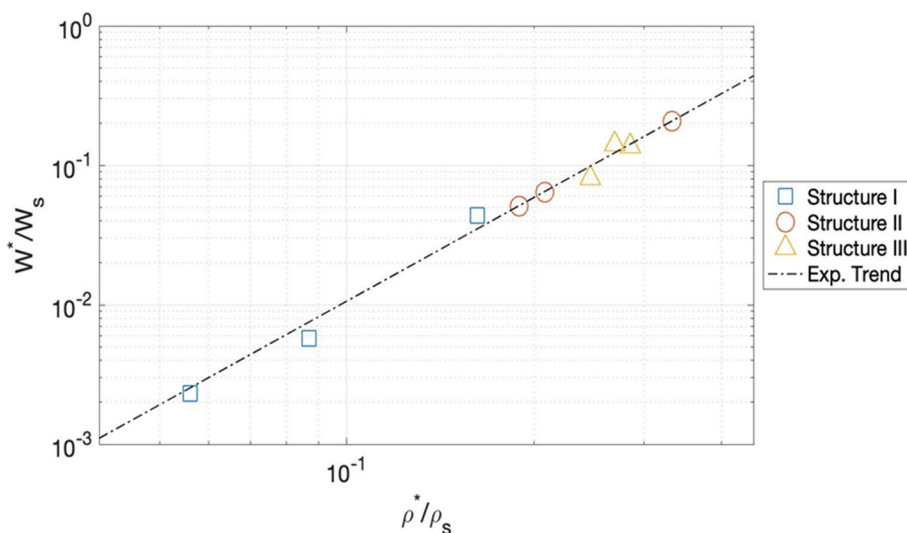


Table 5 Comparisons between some of the collected data with similar values of relative density

Data	Structure	Cell size (mm)	ρ^*/ρ_s (%)	Strut size (mm)	Strut length (mm)	E^* (GPa)
I-4 [32]	Dode Thin	4	16.155	0.297	1.732	0.339
	Rombi Dode	3.75	16.480	0.940	2.540	0.890
II-7 [32]	GStructure 3	7	20.808	1.432	1.884	0.717
	Rombi Dode	3	20.540	0.860	2.070	1.380
II-7 [27]	GStructure 3	7	20.808	1.432	1.884	0.717
	Octet Truss	–	21.000	–	–	4.640
III-7 [32]	Rombi Dode	7	26.859	1.382	2.467	1.285
	Rombi Dode	2.14	26.640	0.770	1.690	2.99
III-7 [19]	Rombi Dode	7	26.859	1.382	2.467	1.285
	Dode Thin	–	28.000	0.800	–	12.900
III-4 [19]	Rombi Dode	4	28.523	0.704	1.410	1.560
	Dode Thin	–	28.000	0.800	–	12.900
III-4 [36, 42]	Rombi Dode	4	28.523	0.704	1.410	1.560
	Cross	2.84	29.680	0.882	2.840	2.130
III-4 [27]	Rombi Dode	4	28.523	0.704	1.410	1.560
	Octet Truss	10	28.500	1.660	–	6.519
B11 b [27]	Rombi Dode	4.29	14.030	1.080	3.130	0.540
	Octet Truss	–	14.000	1.100	–	2.076

relative Young's modulus. Table 5 resumes a more accurate comparison of these results.

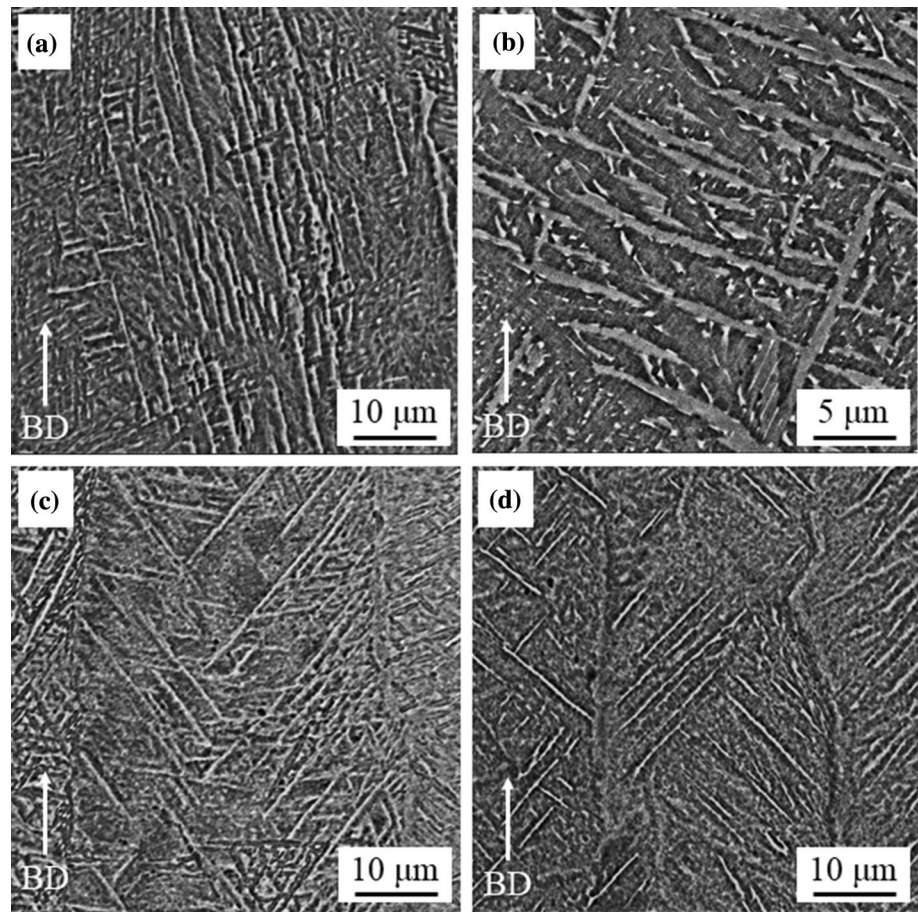
As it can be observed, this finding is in contrast with Ashby and Gibson [24] model (Eq. 5). The differences in mechanical behaviour can be explained by the variation in the cell type, strut size and length and probably surface defects. It should be mentioned that the surface defects which can be developed from the production processes and can also play a key role, is not considered in the Ashby and Gibson model. This suggests that, differently from the foams, lattice structures may exhibit a shape effect based on the singular effects of the just cited geometrical features.

3.2 Microstructure Analysis

To study the mechanical performance of the lattice structures more in details, a microstructure analysis has been carried out. In general, AM technology has lots of merits, but the mechanism of manufacturing, which includes melting of metallic powder followed by solidification has implications for the microstructure of as-built parts. In fact, the rapid and directional solidification phenomena during the AM processes can define the local microstructure. For instance, directional solidification can lead to the formation of preferred crystallographic orientation and consequently change the mechanical characteristics of the component. On the other hand, grain refinement is a direct consequence of rapid solidification that can improve the mechanical properties of the material through the hindering the dislocation motion. However, it should also be noted that this rapid solidification can also result in segregation phenomena or the formation of

non-equilibrium phases. In general, according to the nature of the AM technologies which are categorized as the rapid solidification processes, the presence of a hexagonally-packed acicular martensitic phase microstructure, α' , in the as-built Ti–6Al–4V lattice structures produced via AM process can be expected [19, 27]. However, Fig. 14 shows the typical microstructure for the as-built sample produced via EBM, which includes of α -acicular phase (also known as Widmanstätten platelet structure) surrounded by β phase. As mentioned earlier, in the case of small volume parts, the transformation from the elevated temperature β phase to low-temperature α -phase can occur diffusionless and leads to the formation of martensitic α' -titanium. This finding is in line with the outcomes of previous works [19, 27]. However, due to the presence of the preheating phase and also reheating the already solidified layer during the melting of a new layer in the EBM process, this α' martensitic phase is decomposed to α and β . In addition, Fig. 14a, b shows the SEM image of a surface parallel to the building direction for the structure I with 4 mm strut size. This image shows the typical microstructure of EBM Ti–6Al–4V, which includes columnar grains of prior β growing epitaxially in the building direction (BD) and Widmanstätten α platelets. It is also found that the width of these columnar grains lies in the range of 70–150 μm . Moreover, it is revealed that the microstructure within the columnar grains of the β phase includes typical $\alpha + \beta$ such as the Widmanstätten α platelets with various sizes and orientations. Figure 14b shows the higher magnification of Fig. 14a, which reveals the α and β phase ($\sim 2.3\%$). Indeed, in this image the phase with the high contrast is β phase which is enriched in a heavy element

Fig. 14 SEM images of design I-4 (a, b), I-7 c, and I-10 d



like Vanadium. Figure 14c, d show the microstructure of a surface parallel to the building direction for the structure I with strut size of 7 and 10 mm, respectively. As can be seen the microstructures of those three different lattice structures with different strut sizes are rather identical and the thickness of their α platelets lines in the range of 1–2 μm . This finding implies that the variation of strut size has no effect on the microstructure of the lattice structures.

As can be seen in Fig. 14b, the β phase with the line shape was revealed along with the α platelets and at the interface of two platelets. This phase composition of the alloy in the as-built state was found to be very effective in the strengthening of the alloy with sacrificing the ductility of the materials. This contradictory effects of the phase composition on the mechanical characteristics can also play a role in the deformation of the alloy during the compression test and changing the fracture mode of

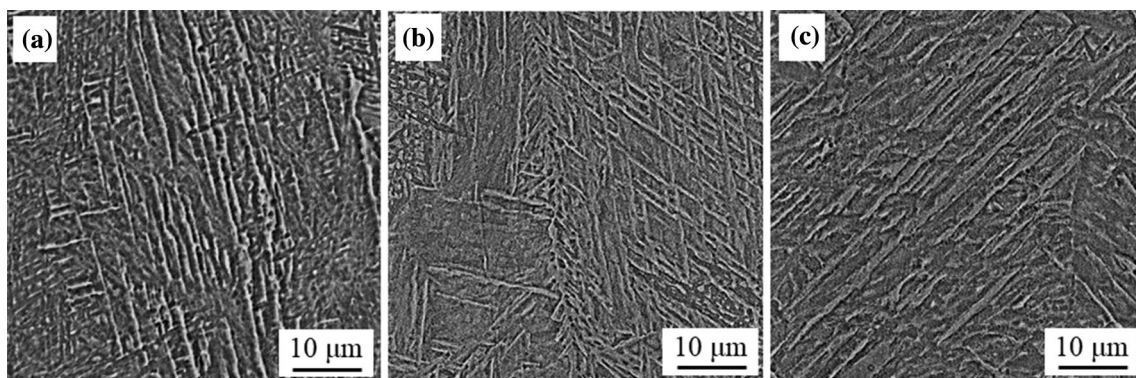


Fig. 15 SEM images of the lattice structure a I, b II and c III with strut size of 4 mm

the samples from a ductile fracture to a brittle one. Figure 15a–c presents the SEM images of the lattice structure I, II and III with strut size of 4 mm. It is very interesting to note that, at the same strut size, despite the presence of rather similar microstructure in all the structures, the thickness of α platelets is slightly increased for the structure II and III and lies in the range of 2–3 μm . This variation in the lath thickness could be related to the thermal history of the sample during the building process. Nonetheless, Fig. 15 shows that the type of cell has not a marked effect of the microstructure of the Ti–6Al–4V EBM lattice structures.

4 Conclusions

In the present study, the effect of different cell types and sizes on the compressive behaviour and microstructure of lattice structures made of Ti–6Al–4V alloy has been carried out. The Ti–6Al–4V lattice structures have been produced by an EBM system using standard parameters provided by Arcam Ab. The main findings of this work can be summarised as follows:

- Beyond the typology and the size of the cell, the relative density of the structure is one of the main factors that influence the mechanical behaviour the lattice structures.
- The increasing trend of Young's modulus and the Ultimate Compressive Strength by increasing the relative density was in line with the prediction of Ashby and Gibson model.
- For the first time, also the absorbed energy up to failure has been demonstrated to be closely correlated to the relative density. Alike of Ashby-Gibson relationship has been found between relative absorbed energy and the relative density.
- The typical microstructure for the as-built Ti–6Al–4V sample produced via EBM, which includes of α -acicular phase (also known as Widmanstätten platelet structure) surrounded by β phase was found in the as-built lattice samples.
- The contradictory effects of the phase composition of the as-built Ti–6Al–4V lattice samples produced via EBM on their mechanical characteristics can also play a role in the deformation of the alloy during the compression test.
- The microstructural analysis shows that cell type and cell size has a negligible effect on the microstructure of lattice specimens.
- The comparisons between the experimental data of the presented work and the data in the literature indicated

that the lattice structures with similar relative density do not exhibit Young's modulus values. This consideration open to exploit new approaches for describing and predicting the mechanical behaviour of the lattice structures which consider not only their relative density but also consider their geometrical feature as well as their microstructural features.

Author Contributions GDG: Experiment, data collection, Writing the first draft, MG: Data Curation, Investigation, Writing—review and editing, Supervision, AS: Conceptualization, Investigation, Validation, Writing—review and editing, Supervision.

Funding The authors received no specific funding for this work.

Compliance with Ethical Standards

Conflict of interest The authors declare that they have no conflict of interest.

References

1. ASTM, *F2792–12a—Standard Terminology for Additive Manufacturing Technologies* (Rapid Manuf. Assoc., 2013), pp. 10–12.
2. A. Saboori, D. Gallo, S. Biamino, P. Fino, M. Lombardi, An Overview of additive manufacturing of titanium components by Directed Energy Deposition: microstructure and mechanical properties. *Appl. Sci.* **7**, 883 (2017)
3. A. Saboori, G. Piscopo, M. Lai, A. Salmi, S. Biamino, An investigation on the effect of deposition pattern on the microstructure, mechanical properties and residual stress of 316L produced by Directed Energy Deposition. *Mater. Sci. Eng. A* **780**, 139179 (2020)
4. I. Gibson, D.W. Rosen, B. Stucker, *Additive Manufacturing Technologies*, vol. 17 (Springer, Berlin, 2014)
5. A. Saboori et al., Production of single tracks of Ti–6Al–4V by Directed Energy Deposition to determine the layer thickness for multilayer deposition. *J. Vis. Exp.* **2018**(133), e56966 (2018)
6. A. Saboori, A. Aversa, G. Marchese, S. Biamino, M. Lombardi, P. Fino, Application of Directed Energy Deposition-based additive manufacturing in repair. *Appl. Sci.* **9**(16), 3316 (2019)
7. M. Aristizabal, P. Jamshidi, A. Saboori, S.C. Cox, M.M. Attallah, Laser powder bed fusion of a Zr-alloy: tensile properties and biocompatibility. *Mater. Lett.* **259**, 126897 (2020)
8. A. Saboori et al., An investigation on the effect of powder recycling on the microstructure and mechanical properties of AISI 316L produced by Directed Energy Deposition. *Mater. Sci. Eng. A* **766**, 138360 (2019)
9. G. Del Guercio, M. Galati, A. Saboori, P. Fino, L. Iuliano, Microstructure and mechanical performance of Ti–6Al–4V lattice structures manufactured via electron beam melting (EBM): a review. *Acta Metall. Sin. (Engl. Lett.)* **33**(2), 183–203 (2020)
10. A. Saboori et al., Characterization of single track formation from Ti–6Al–4V alloy at different process parameters by Direct Energy Deposition, in *Euro PM2017 Congress & Exhibition*, 2017, pp. 1–5.

11. F. Calignano, M. Galati, L. Iuliano, P. Minetola, Design of additively manufactured structures for biomedical applications: a review of the additive manufacturing processes applied to the biomedical sector. *J. Healthc. Eng.* **2019**, 1–6 (2019).
12. M. Galati, A. Snis, L. Iuliano, Experimental validation of a numerical thermal model of the EBM process for Ti6Al4V. *Comput. Math. Appl.* **78**, 2417–2427 (2018)
13. A. Mitchell, Melting, casting and forging problems in titanium alloys. *Mater. Sci. Eng. A* **243**(1–2), 257–262 (1998)
14. H. Galarraga, R.J. Warren, D.A. Lados, R.R. Dehoff, M.M. Kirka, P. Nandwana, Effects of heat treatments on microstructure and properties of Ti–6Al–4V ELI alloy fabricated by electron beam melting (EBM). *Mater. Sci. Eng. A* **685**, 417–428 (2017)
15. M. Galati, P. Minetola, G. Rizza, Surface roughness characterisation and analysis of the electron beam melting (EBM) process. *Materials (Basel)* **12**(13), 2211 (2019)
16. W. He, W. Jia, H. Liu, H. Tang, X. Kang, Y. Huang, Research on preheating of titanium alloy powder in electron beam melting technology. *Xiyou Jinshu Cailiao Yu Gongcheng/Rare Met. Mater. Eng.* **40**(12), 2072–2075 (2011)
17. N.A. Fleck, V.S. Deshpande, M.F. Ashby, Micro-architected materials: Past, present and future. *Proc. R. Soc. A Math. Phys. Eng. Sci.* **466**(2121), 2495–2516 (2010)
18. A.G. Evans, J.W. Hutchinson, M.F. Ashby, Multifunctionality of cellular metal systems. *Prog. Mater. Sci.* **43**(3), 171–221 (1998)
19. L.E. Murr et al., Next-generation biomedical implants using additive manufacturing of complex, cellular and functional mesh arrays. *Philos. Trans. R. Soc. A Math. Phys. Eng. Sci.* **368**(1917), 1999–2032 (2010)
20. M. Niinomi, Recent metallic materials for biomedical applications. *Metall. Mater. Trans. A* **33**(3), 477 (2002)
21. J.-W. Park, H.-K. Kim, Y.-J. Kim, J.-H. Jang, H. Song, T. Hanawa, Osteoblast response and osseointegration of a Ti–6Al–4V alloy implant incorporating strontium. *Acta Biomater.* **6**(7), 2843–2851 (2010)
22. M.F. Ashby, The properties of foams and lattices. *Philos. Trans. R. Soc. A Math. Phys. Eng. Sci.* **364**(1838), 15–30 (2006)
23. J.C. Maxwell, L. on the calculation of the equilibrium and stiffness of frames. *Lond. Edinb. Dublin Philos. Mag. J. Sci.* **27**(182), 294–299 (1864)
24. L.J. Gibson, M.F. Ashby, *Cellular Solids: Structure and Properties* (Cambridge University Press, Cambridge, 1999)
25. H.R. Vladimir Popov, A. Katz-Demyanetz, A. Garkun, G. Muller, E. Strokin et al., Effect of hot isostatic pressure treatment on the electron-beam melted Ti–6Al–4V specimens. *Procedia Manuf.* **21**, 125–132 (2018)
26. C. De Formanoir, S. Michotte, O. Rigo, L. Germain, S. Godet, Electron beam melted Ti–6Al–4V: Microstructure, texture and mechanical behavior of the as-built and heat-treated material. *Mater. Sci. Eng. A* **652**, 105–119 (2016)
27. C. de Formanoir, M. Suard, R. Dendievel, G. Martin, S. Godet, Improving the mechanical efficiency of electron beam melted titanium lattice structures by chemical etching. *Addit. Manuf.* **11**, 71–76 (2016)
28. Y. Zhai, H. Galarraga, D.A. Lados, Microstructure evolution, tensile properties, and fatigue damage mechanisms in Ti–6Al–4V alloys fabricated by two additive manufacturing techniques. *Procedia Eng.* **114**, 658–666 (2015)
29. R. Cunningham et al., Analyzing the effects of powder and post-processing on porosity and properties of electron beam melted Ti–6Al–4V. *Mater. Res. Lett.* **5**(7), 516–525 (2017)
30. K.S. Chan, M. Koike, R.L. Mason, T. Okabe, Fatigue life of titanium alloys fabricated by additive layer manufacturing techniques for dental implants. *Metall. Mater. Trans. A* **44**(2), 1010–1022 (2013)
31. S.J. Li et al., Compression fatigue behavior of Ti–6Al–4V mesh arrays fabricated by electron beam melting. *Acta Mater.* **60**(3), 793–802 (2012)
32. X.Y. Cheng et al., Compression deformation behavior of Ti–6Al–4V alloy with cellular structures fabricated by electron beam melting. *J. Mech. Behav. Biomed. Mater.* **16**, 153–162 (2012)
33. W. van Grunsven, E. Hernandez-Nava, G. Reilly, R. Goodall, Fabrication and mechanical characterisation of titanium lattices with graded porosity. *Metals (Basel)* **4**(3), 401–409 (2014)
34. M. Jamshidinia, L. Wang, W. Tong, R. Kovacevic, The bio-compatible dental implant designed by using non-stochastic porosity produced by electron beam melting®(EBM). *J. Mater. Process. Technol.* **214**(8), 1728–1739 (2014)
35. L. Xiao, W. Song, C. Wang, H. Liu, H. Tang, J. Wang, Mechanical behavior of open-cell rhombic dodecahedron Ti–6Al–4V lattice structure. *Mater. Sci. Eng. A* **640**, 375–384 (2015)
36. J. Parthasarathy, B. Starly, S. Raman, A. Christensen, Mechanical evaluation of porous titanium (Ti6Al4V) structures with electron beam melting (EBM). *J. Mech. Behav. Biomed. Mater.* **3**(3), 249–259 (2010)
37. O. Cansizoglu, O. Harrysson, D. Cormier, H. West, T. Mahale, Properties of Ti–6Al–4V non-stochastic lattice structures fabricated via electron beam melting. *Mater. Sci. Eng. A* **492**(1–2), 468–474 (2008)
38. L. Xiao et al., Mechanical properties of open-cell rhombic dodecahedron titanium alloy lattice structure manufactured using electron beam melting under dynamic loading. *Int. J. Impact Eng.* **100**, 75–89 (2017)
39. M. Suard, P. Lhuissier, R. Dendievel, J.-J. Blandin, F. Vignat, F. Villeneuve, Towards stiffness prediction of cellular structures made by electron beam melting (EBM). *Powder Metall.* **57**(3), 190–195 (2014)
40. T.J. Horn, O.L.A. Harrysson, D.J. Marcellin-Little, H.A. West, B.D.X. Lascelles, R. Aman, Flexural properties of Ti6Al4V rhombic dodecahedron open cellular structures fabricated with electron beam melting. *Addit. Manuf.* **1**, 2–11 (2014)
41. E. Hernández-Nava et al., The effect of density and feature size on mechanical properties of isostructural metallic foams produced by additive manufacturing. *Acta Mater.* **85**, 387–395 (2015)
42. J. Parthasarathy, B. Starly, S. Raman, A design for the additive manufacture of functionally graded porous structures with tailored mechanical properties for biomedical applications. *J. Manuf. Process.* **13**(2), 160–170 (2011)
43. L.E. Murr et al., Characterization of Ti–6Al–4V open cellular foams fabricated by additive manufacturing using electron beam melting. *Mater. Sci. Eng. A* **527**(7), 1861–1868 (2010)
44. Arcam, *Ti6Al4V Titanium Alloy* (Arcam AB, Mölndal, Sweden, 2014), pp. 4–6.

Publisher's Note Springer Nature remains neutral with regard to jurisdictional claims in published maps and institutional affiliations.